RSC Advances

PAPER

View Article Online
View Journal | View Issue

Open Access Article. Published on 13 July 2022. Downloaded on 11/8/2025 5:17:05 AM.
This article is licensed under a Creative Commons Attribution-NonCommercial 3.0 Unported Licence.

Check for updates

Cite this: *RSC Adv.*, 2022, **12**, 20395

Tailor-designed nanowire-structured iron and nickel oxides on platinum catalyst for formic acid electro-oxidation

Bilquis Ali Al-Qodami,[ab] Hafsa H. Alalawy, *[a] Sayed Youssef Sayed, [a] Islam M. Al-Akraa, [c] Nageh K. Allam [d] and Ahmad M. Mohammad *[a]

This investigation is concerned with designing efficient catalysts for direct formic acid fuel cells. A ternary catalyst containing iron (nano-FeO*x*) and nickel (nano-NiO*x*) nanowire oxides assembled sequentially onto a bare platinum (bare-Pt) substrate was recommended for the formic acid electro-oxidation reaction (FAOR). While nano-NiO*x* appeared as fibrillar nanowire bundles (*ca.* 82 nm and 4.2 μm average diameter and length, respectively), nano-FeO*x* was deposited as intersecting nanowires (*ca.* 74 nm and 400 nm average diameter and length, respectively). The electrocatalytic activity of the catalyst toward the FAOR depended on its composition and loading sequence. The FeO*x*/NiO*x*/Pt catalyst exhibited *ca.* 4.8 and 1.6 times increases in the catalytic activity and tolerance against CO poisoning, respectively, during the FAOR, relative to the bare-Pt catalyst. Interestingly, with a simple activation of the FeO*x*/NiO*x*/Pt catalyst at −0.5 V *vs.* Ag/AgCl/KCl (sat.) in 0.2 mol L^{-1} NaOH, a favorable Fe^{2+}/Fe^{3+} transformation succeeded in mitigating the permanent CO poisoning of the Pt-based catalysts. Interestingly, this activated a-FeO*x*/NiO*x*/Pt catalyst had an activity 7 times higher than that of bare-Pt with an *ca.* −122 mV shift in the onset potential of the FAOR. The presence of nano-FeO*x* and nano-NiO*x* enriched the catalyst surface with extra oxygen moieties that counteracted the CO poisoning of the Pt substrate and electronically facilitated the kinetics of the FAOR, as revealed from CO stripping and impedance spectra.

Received 31st May 2022
Accepted 15th June 2022

DOI: 10.1039/d2ra03386k

rsc.li/rsc-advances

1. Introduction

Society is currently confronted with a difficult task; replacing traditional fossil fuels with renewable resources. Direct liquid fuel cells (DLFCs) have sparked widespread interest in research and industry as a very promising technology for resolving the worldwide environmental and energy crises.[1,2] Among the several studied fuel cells (FCs), direct formic acid fuel cells (DFAFCs) appear to be promising as alternative power sources for portable electronic applications and in transportation due to their high energy density (∼1.4 kWh kg^{-1}), high theoretical open circuit potential (OCP ∼ 1.48 V), fast oxidation kinetics and cell efficiency.[3,4] This is in addition to the utilization of a superior liquid fuel with high safety, low toxicity, low-flammability, ready availability, ambient temperature operability and low fuel crossover flux through Nafion membranes.[5–9]

The most significant factors that influence the final output of DFAFCs are the electrocatalysts for both the anode and cathode electrodes, where Pt and Pd-based catalysts have been extensively studied due to their outstanding catalytic activity and long-term stability.[7,10] Formic acid (FA) is one of the smallest organic molecules likely to be used, with only two electrons shared. Thus, it has been used as a model molecule in the study of the oxidation of other organic compounds with more intricate structures and oxidation mechanisms. Despite several efforts devoted to the research of the oxidation of these compounds, the overpotentials of the oxidation reaction are still far too high for large-scale practical application. Therefore, better electrocatalysts with lower overpotentials should be developed in order to optimize the fuel cell system's overall energy efficiency.[11] The reaction mechanism is an important piece of knowledge for the development of improved electrocatalysts. Knowing the intricacies of the reaction process will allow the development of new electrode materials able to speed up the reaction's slowest steps, allowing the reaction bottlenecks to be overcome and higher efficiencies to be achieved.[3,11] Because only two electrons are exchanged, the FA oxidation reaction (FAOR) is a comparatively simple reaction. In fact, only the cleavage of two bonds is needed for full oxidation to CO_2: an O–H bond and an H–C bond. This second cleavage is possibly the most difficult stage, but pure metals (such as Pt, Pd and Ru)

[a]Chemistry Department, Faculty of Science, Cairo University, Cairo 12613, Egypt. E-mail: hafsa@sci.cu.edu.eg; ammohammad@cu.edu.eg

[b]Chemistry Department, Faculty of Education and Applied Science, Hajjah University, Yemen

[c]Department of Chemical Engineering, Faculty of Engineering, The British University in Egypt, Cairo 11837, Egypt

[d]Energy Materials Laboratory, School of Sciences and Engineering, The American University in Cairo, New Cairo 11835, Egypt

© 2022 The Author(s). Published by the Royal Society of Chemistry

Open Access Article. Published on 13 July 2022. Downloaded on 11/8/2025 5:17:05 AM.
This article is licensed under a Creative Commons Attribution-NonCommercial 3.0 Unported Licence.

are active for this stage because of their excellent properties for hydrogen adsorption.[11,12] However, when this reaction was examined on platinum, a poisoning species, such as CO, was found to form. The formation of CO means the existence of unexpected problems in the process of oxidation. Because adsorbed CO is oxidized at high potentials, it prevents the reaction from taking place on the metal surface. Therefore, the oxidation mechanism involves two parallel routes: the direct formation of CO_2 from HCOOH at low potentials through a dehydrogenation step (desirable pathway) ($HCOOH \rightarrow CO_2 + 2H^+ + 2e^-$), and the indirect formation of CO *via* a chemical dehydration step, which will be further oxidized to CO_2 at higher potentials ($HCOOH \rightarrow CO_{ads} + H_2O \rightarrow CO_2 + 2H^+ + 2e^-$).[13–19]

Many catalysts have been reported for the FAOR in alkaline and acidic media. The noble metals are the most used electrocatalysts because of their superior activity. In fact, the FAOR on Pt and Pd electrodes has been the focus of growing interest since the 1960s.[20] This is mostly owing to its importance in understanding methanol and formaldehyde oxidation, as well as the development of DFAFCs. However, difficult issues, such as limited catalytic activity on Pt at low potential, long-term instability (or deactivation) of Pd and Pt catalysts, degradation of carbon supports and the Nafion membrane, and water-CO_2 management in fuel cell stacks, impede DFAFC commercialization on a wide scale. Significant efforts are being made to solve these issues through different approaches, such as developing new designs of DFAFCs and preparing high efficiency anode catalysts.[20,21] Particularly, Pt is regarded as the most suitable electrocatalyst among all metals due to its excellent stability. However, CO poisoning *via* the dehydration pathway of the FAOR on the Pt surface degrades its catalytic activity, reducing its use. The combination of Pt-based intermetallic catalysts may improve the catalytic activity and durability for the FAOR.

In order to enhance the electrocatalytic activity, suppress poisoning by CO and increase the stability of the Pt catalyst toward the FAOR, several metals have been combined with Pt as intermetallic compounds, alloys, adatoms, or core–shell structures. The impact of other metals and/or metal oxides could be demonstrated by ensemble effects, electronic effects or a bi-functional mechanism. In this regard, Pt-based catalysts have made significant progress in direct oxidation activities by surface modification, shape engineering, and alloying with other metals such as Pd, Au, Cu, *etc.*[6,20,22,23] Many other studies have been performed in order to use binary catalysts, such as PtM (M = Au,[24,25] Bi,[14] Co,[26] Cu,[27] Ni,[28] Rh,[29] Sn,[30] Fe,[31] Zr,[32] Nb,[33] *etc.*) and ternary catalysts such as PtM1M2 (M1M2 = RuAu,[34] PdCu,[35] CuFe,[36] SnBi,[6] AuCu [37] and BiPd [7]). Furthermore, when modifying Pt surfaces with transition metal oxide nanostructures (MO*x*), such as NiO*x*,[38,39] CoO*x*,[40] TiO*x*,[41] MnO*x*,[42,43] Cu_2O,[44] FeO*x*,[45,46] *etc.*, the catalytic improvement achieved toward the FAOR was motivated by the so-called "bi-functional effect", where the required oxygen atmosphere could easily be supplied by non-precious metal/s to facilitate the CO stripping at low overpotentials. Pt surface modification may also facilitate a change in the Pt work function in both circumstances (ensemble and bi-functional effects) to provide controlled tuning for Pt-FA and Pt–CO binding. In this study, the activity and stability of a new FeO*x*/NiO*x*/Pt catalyst for the FAOR was studied. The Pt surface was amended with peerless cheap and abundant metal oxides (FeO*x* and NiO*x*) that could effectively boost the kinetics of the FAOR and minimize the surface poisoning of Pt to allow DFAFCs to be scaled for practical use.

2. Experimental

2.1. Chemicals

All chemicals utilized in this work were of analytical grade and were used as received, with no prior purification. All solutions were prepared with double-distilled water. Nickel sulfate hexahydrate ($NiSO_4 \cdot 6H_2O$), formic acid (HCOOH, FA), disodium hydrogen phosphate (Na_2HPO_4), hydrochloric acid (HCl), sodium hydroxide pellets (NaOH) and sulfuric acid (H_2SO_4) were purchased from Sigma-Aldrich, whereas iron(II) sulfate heptahydrate ($FeSO_4 \cdot 7H_2O$) and sodium sulfate (Na_2SO_4) were purchased from Riedel-de Haën and Merck, respectively.

2.2. Electrochemical measurements

Electrochemical tests, such as cyclic voltammetry (CV), chronoamperometry (CA), and electrochemical impedance spectroscopy (EIS), were performed in a constructed two-compartment three-electrode Pyrex glass cell. Polycrystalline platinum ($d = 3.0$ mm), platinum spiral wire and Ag/AgCl/KCl (sat.) served as the working, counter and reference electrodes, respectively. Even if not stated, all the potential readings in this study were taken in reference to the Ag/AgCl/KCl (sat.) electrode. All measurements were performed at room temperature (25 ± 1 °C) using an EG&G potentiostat (model 273) operated with E-Chem 270 software.

2.3. Catalyst preparation

The polycrystalline bare "pristine" Pt (bare-Pt or poly-Pt) electrode was mechanically polished with aqueous slurries of successively finer alumina powder, and subsequently sonicated and washed with double-distilled water. Then, the poly-Pt electrode was further electrochemically cleaned in 0.5 mol L^{-1} H_2SO_4 solution by cycling the potential between −0.2 and 1.3 V at 100 mV s^{-1} until a characteristic CV for a clean poly-Pt electrode was obtained. The electrode modification with nickel oxide nanostructures (nano-NiO*x*) was achieved in three sequential steps. The first corresponded to the electrodeposition of metallic nickel (Ni) from 0.1 mol L^{-1} Na_2SO_4 solution containing 1.0 mmol L^{-1} $NiSO_4 \cdot 6H_2O$ at a constant potential of −1.0 V for 120 s.[38,39] After that, the metallic nickel was passivated to nickel oxide by cycling the potential from −0.5 to 1 V at 200 mV s^{-1} in 0.1 mol L^{-1} phosphate buffer solution (PBS, pH 7, prepared from 0.1 mol L^{-1} Na_2HPO_4 and 0.1 mol L^{-1} HCl). Finally, the as-prepared electrode was activated by cycling the potential between −1 and 0.6 V at a scan rate of 200 mV s^{-1} for 25 cycles in 0.5 mol L^{-1} NaOH solution.

Fig. 1 exhibits CVs of 10 potential cycles in PBS (pH 7) for the passivation of deposited metallic Ni on the bare-Pt electrode.

 © 2022 The Author(s). Published by the Royal Society of Chemistry

Open Access Article. Published on 13 July 2022. Downloaded on 11/8/2025 5:17:05 AM.
This article is licensed under a Creative Commons Attribution-NonCommercial 3.0 Unported Licence.

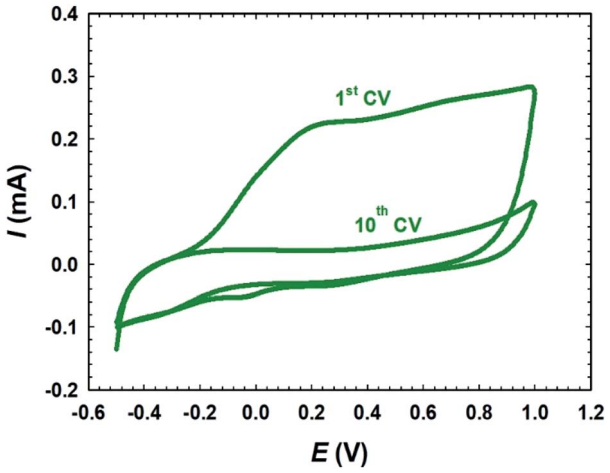

Fig. 1 CVs of the passivation of the electrodeposited metallic Ni on the bare-Pt electrode in 0.1 mol L^{-1} PBS (pH 7.0).

For simplicity, only the first and tenth voltammograms are shown. A broad oxidative wave in the 1st CV corresponded to the active anodic dissolution and passivation of the electrodeposited metallic Ni synchronised between the various phases of nickel oxides. The following consecutive 9 CVs revealed a negligible anodic current, indicating a complete passivation of the surface layer of nickel during the first CV cycle. Interestingly, the absence of any significant reduction peaks in the cathode scan within the suitable potential domain indicated that the passive NiO*x* nanoparticles were stable within the potential range used and the specified pH. The electrodeposition of iron species was carried out by potential cycling (2 cycles) between −0.855 and −1.205 V at a scan rate of 100 mV s^{-1} in 0.02 mol L^{-1} $FeSO_4 \cdot 7H_2O$ solution. Next, the deposited iron was activated in 0.2 mol L^{-1} NaOH aqueous solution at −0.5 V for 10 min, where iron oxide nanorods (nano-FeO*x*) were formed.[45,46] To easily recognize the sequencing of the different catalytic ingredients and the post-treatment of the catalyst, abbreviations related to their developments were assigned. For instance, the a-FeO*x*/NiO*x*/Pt catalyst referred to the direct deposition of nano-NiO*x* onto the bare-Pt substrate followed by its passivation and activation. Then, nano-FeO*x* was deposited later onto the NiO*x*/Pt catalyst. The prefix "a-" denoted the further activation of nano-FeO*x* as described previously.

2.4. Materials characterization

The morphology and surface composition of the as-prepared Pt-based electrocatalysts were characterized by field-emission scanning electron microscopy (FE-SEM, Zeiss Ultra 60), at an acceleration voltage of 8 kV and a working distance of 2.8–3.2 mm, coupled with an energy dispersive X-ray spectrometer (EDX).

3. Results and discussion

3.1. Electrochemical and materials characterization

The electrochemical characterization was first used to detect the nature of the electroactive species on the various modified Pt electrodes. Fig. 2A compares CVs of the unmodified (a) bare-Pt and modified (b–f) NiO*x*/Pt, FeO*x*/NiO*x*/Pt, a-FeO*x*/NiO*x*/Pt, NiO*x*/FeO*x*/Pt and NiO*x*/a-FeO*x*/Pt catalysts, respectively, in 0.5 mol L^{-1} NaOH solution. As can be clearly seen, the CV of the Pt electrode (curve a) exhibited typical characteristics of a clean poly-Pt electrode, with two peaks for the $H_{ads/des}$ in the potential range from −1.0 to −0.65 V, together with another peak couple for the PtO/Pt transformation at −0.40 V. After modifying the Pt electrode with nano-NiO*x*, well-defined redox peaks at 0.32 and 0.42 V, corresponding to the Ni(II)/Ni(III) reversible transformation, were seen.[38,39,47,48] In addition, a significant decrease was observed in the Pt surface area, which can easily be estimated from the lower peak intensities of the PtO reduction, Pt oxidation and $H_{ads/des}$ peaks (curve b). A further modification with nano-FeO*x* resulted in the emergence of the distinctive well-defined redox peaks for $Fe^{2+} \leftrightarrow Fe^{3+}$ at *ca.* −0.63 V (anodic scan) and −0.83 V (cathodic scan), curve c.[49] Interestingly, the

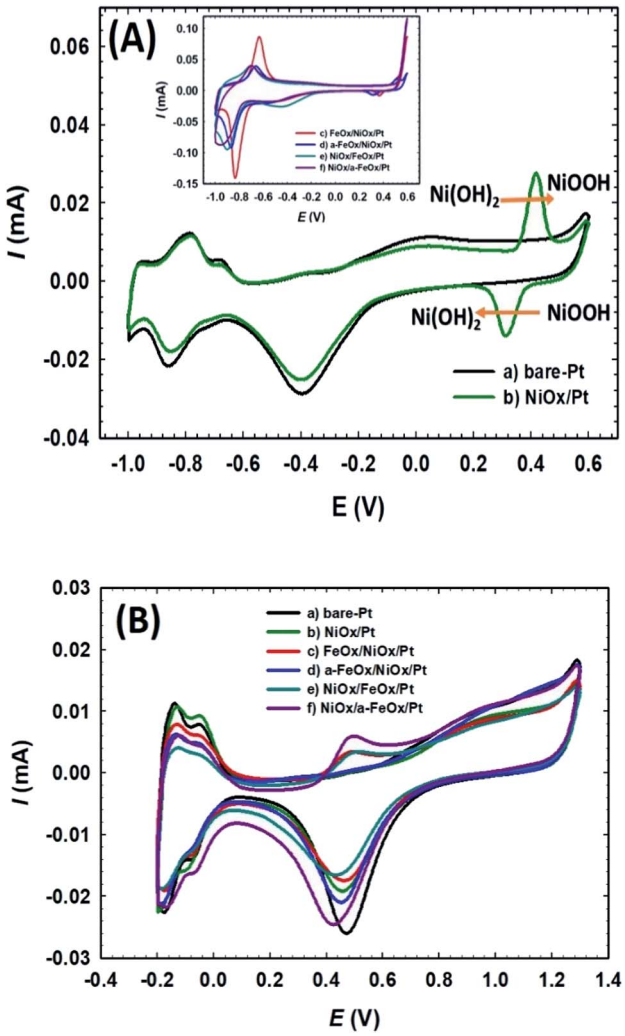

Fig. 2 CVs obtained in 0.5 mol L^{-1} NaOH (A) and in 0.5 mol L^{-1} H_2SO_4 (B) for: (a) bare-Pt, (b) NiO*x*/Pt, (c) FeO*x*/NiO*x*/Pt, (d) a-FeO*x*/NiO*x*/Pt, (e) NiO*x*/FeO*x*/Pt and (f) NiO*x*/a-FeO*x*/Pt catalysts at a scan rate of 200 mV s^{-1}.

Open Access Article. Published on 13 July 2022. Downloaded on 11/8/2025 5:17:05 AM.
This article is licensed under a Creative Commons Attribution-NonCommercial 3.0 Unported Licence.

existence of nano-FeO*x* in the catalyst, regardless of its deposition order, led to a significant boosting of the oxygen evolution reaction (OER), as seen at *ca.* 0.55 V. The presence of the OER peak was clearly caused by the existence of the nano-FeO*x* and nano-NiO*x* together in the catalyst, but it did not appear in the case of either the NiO*x*/Pt (curve b) or Pt (curve a) electrodes at, or before, *ca.* 0.55 V. The redox peak for the Fe^{2+}/Fe^{3+} transformation was observed with the a-FeO*x*/NiO*x*/Pt (−0.5 V) catalyst, with small negative shifts in the potential (−0.66 to −0.87 V, curve d). The same behaviour was retained with the NiO*x*/FeO*x*/Pt (curve e) and NiO*x*/a-FeO*x*/Pt (curve f) catalysts, but the Fe^{2+}/Fe^{3+} peaks were shifted to higher negative potentials.

Fig. 2B shows the CVs for the same catalysts recorded in 0.5 mol L^{-1} H_2SO_4 aqueous solution. The $H_{ads/des}$ peaks, together with those of Pt → PtO oxidation and PtO → Pt reduction, were clearly seen for all catalysts. The polycrystalline nature of Pt was verified from the splitting of the $H_{ads/des}$ peaks. The deposition of nano-NiO*x* and/or nano-FeO*x* on the Pt electrode reduced the exposed surface of the Pt, as inferred from the intensities of the $H_{ads/des}$ and PtO/Pt peaks. The addition of nano-FeO*x* to the NiO*x*/Pt electrode resulted in the appearance of a well-defined redox peak couple in the region of 0.4 to 0.6 V, which might be attributed to Fe^{2+}/Fe^{3+} conversions.[50] This peak couple was almost absent for NiO*x*/Pt and a-FeO*x*/NiO*x*/Pt, but appeared for other catalysts. The absence of this peak in the case of a-FeO*x*/NiO*x*/Pt might be attributed to the detachment or phase transformation of FeO*x* on the Pt surface. After adding the modifiers (nano-NiO*x* and/or nano-FeO*x*) to Pt, the PtO/Pt peak shifted in the negative direction, especially in the case of the deposition of nano-FeO*x* underneath nano-NiO*x* (NiO*x*/FeO*x*/Pt and NiO*x*/a-FeO*x*/Pt electrodes), with an obvious overlapping of the PtO/Pt and Fe^{3+}/Fe^{2+} reduction peaks. The $H_{ads/des}$ peaks with a monolayer adsorption charge of $H_{ads/des}$ of 210 μC cm^{-2} at the Pt surfaces was, for accuracy purposes, used to compute the specific surface area of the catalyst,[51] instead of the PtO → Pt peak, which might be overlapping with other reduction peaks of iron oxides.

FE-SEM imaging revealed the morphological characterization of the modified Pt electrodes. Fig. 3 shows typical FE-SEM micrographs of Pt before (a) and after (b, c and d) modification. The image of the NiO*x*/Pt (Fig. 3b) electrode showed that nano-NiO*x* was electrodeposited on the Pt surface in fibrillar nanowire bundles, with an average diameter of *ca.* 82 nm and length of 4.2 μm. However, the nano-FeO*x* was electrodeposited on the NiO*x*/Pt electrode in intersected nanowires, with an average diameter of *ca.* 74 nm and length of 400 nm (Fig. 3c). Interestingly, the activation led to the emergence of many aggregates of nanowires (Fig. 3d). The elemental composition of the FeO*x*/NiO*x*/Pt electrode was identified by the EDX measurement, as shown in Fig. 4. It reflected that the catalyst contained Ni, Fe, O and Pt, with percentages of 9.97, 6.15, 48.51 and 35.37%, respectively. The presence of O at such a high level was probably due to oxide formation, whereas the high extent of Pt resulted from the bare-Pt substrate. This indicated the successful deposition of the catalyst's ingredients.

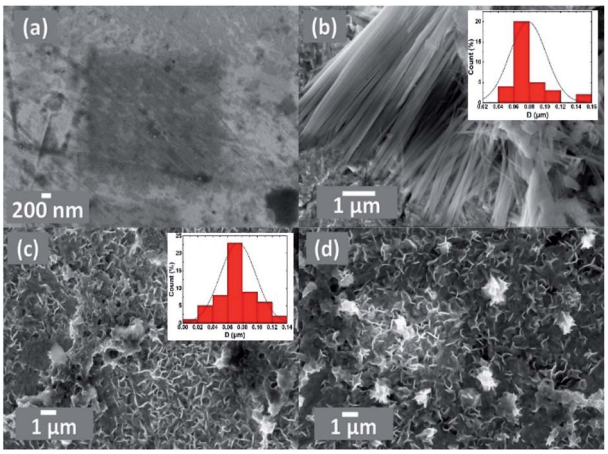

Fig. 3 FE-SEM images of the (a) bare-Pt, (b) NiO*x*/Pt, (c) FeO*x*/NiO*x*/Pt and (d) a-FeO*x*/NiO*x*/Pt electrodes. The insets in (b) and (c) are the particle size distribution histograms of NiO*x*/Pt and FeO*x*/NiO*x*/Pt.

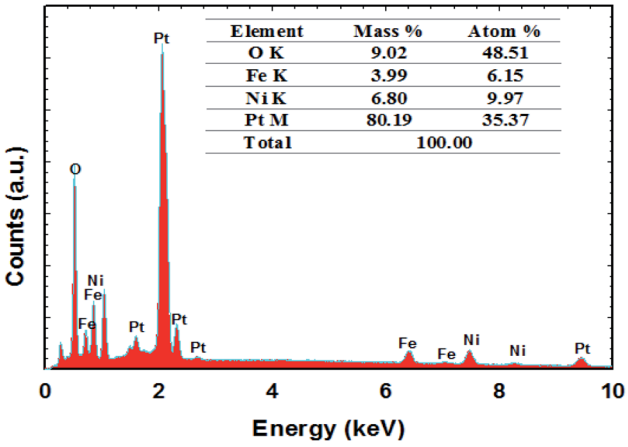

Fig. 4 The EDX spectrum of the FeO*x*/NiO*x*/Pt catalyst.

3.2. Electrocatalysis of the FAOR

The electrocatalytic performance of the modified electrodes toward the FAOR was investigated by recording CVs in 0.3 mol L^{-1} FA (pH 3.5) at a scan rate of 200 mV s^{-1} in the potential range from −0.2 to 1.0 V, (Fig. 5). It is worth mentioning that the stability of iron and nickel oxides decreases in highly acidic solutions.[39,52] Therefore, the present study was conducted in a slightly acidic medium, pH = 3.5, located within the iron and nickel oxides' stability domains. Additionally, a large (about one-third) amount of FA is ionized at this pH to formate anions.[44] As such, the ionic conductivity is expected to be improved, along with a lower solution resistance.[38,39] In general, there are two mechanisms suggested for the FAOR, as follows:

(1) Direct pathway mechanism:

$$HCOOH \rightarrow H_{(aq)}^{+} + e^{-} + HCOO^{*} \quad (1)$$

$$HCOO^{*} \rightarrow CO_2 + H_{(aq)}^{+} + e^{-} \quad (2)$$

 © 2022 The Author(s). Published by the Royal Society of Chemistry

Open Access Article. Published on 13 July 2022. Downloaded on 11/8/2025 5:17:05 AM.
This article is licensed under a Creative Commons Attribution-NonCommercial 3.0 Unported Licence.

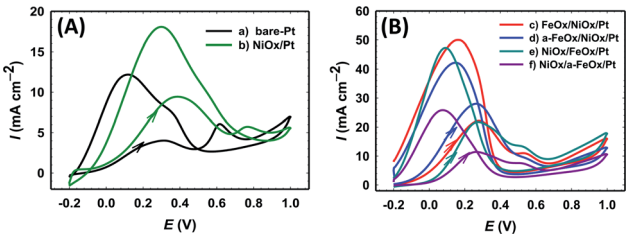

Fig. 5 CVs of the FAOR for the (a) bare-Pt, (b) NiOx/Pt, (c) FeOx/NiOx/Pt, (d) a-FeOx/NiOx/Pt, (e) NiOx/FeOx/Pt and (f) NiOx/a-FeOx/Pt electrodes in 0.3 mol L^{-1} FA (pH 3.5).

(2) Indirect pathway mechanism:

$$HCOOH \rightarrow H_{(aq)}^{+} + e^{-} + COOH^{*} \quad (3)$$

$$COOH^{*} \rightarrow CO^{*} + OH^{*} \quad (4)$$

$$CO^{*} + OH^{*} \rightarrow CO_2 + H^{+} + e^{-} \quad (5)$$

The direct pathway mechanism is dominant at low applied potentials (<0.25 V), resulting in CO_2 formation after two steps of proton/electron transfer, through an HCOO* intermediate (eqn (1) and (2)). The indirect mechanism of the FAOR, prevalent at high applied potentials (>0.6 V), contributes to CO formation through a different intermediate, COOH* (eqn (3) and (4)), and its subsequent oxidation to CO_2 (eqn (5)).[53] The first (direct pathway) and second (indirect pathway) peak currents are symbolized as I_p^d and I_p^{ind} in the forward (positive-going) potential scan, respectively. In the backward scan, the FAOR continues on a clean Pt surface along with Pt dehydroxylation and perhaps CO_2 reduction, but generally the peak current (I_b) is overall anodic. The increase in the intensity of I_p^d concurrent with the decrease of I_p^{ind} indicates that the direct FAOR pathway becomes more favorable. Hence, the ratio of the two oxidation peaks (I_p^d/I_p^{ind}) represents how favorable it is for the FAOR to occur via the direct pathway (or the improvement in the overall catalytic efficiency of the FAOR) for a particular catalyst. Fig. 5 shows the CVs depicting and comparing the specific activities for the bare-Pt, NiOx/Pt, FeOx/NiOx/Pt, a-FeOx/NiOx/Pt, NiOx/FeOx/Pt and NiOx/a-FeOx/Pt catalysts. The I_p^d of the catalysts followed this order: a-FeOx/NiOx/Pt (28.0 mA cm^{-2}) > FeOx/NiOx/Pt (22.0 mA cm^{-2}) > NiOx/FeOx/Pt (21.8 mA cm^{-2}) > NiOx/a-FeOx/Pt (11.5 mA cm^{-2}) > NiOx/Pt (9.0 mA cm^{-2}) > Pt (4.5 mA cm^{-2}). Also, the catalytic activity (assessed using the I_p^d/I_p^{ind} ratio) of the catalysts followed this order: a-FeOx/NiOx/Pt (16.5, which is seven fold higher than that of bare-Pt) > FeOx/NiOx/Pt (11.0) > NiOx/a-FeOx/Pt (9.6) > NiOx/FeOx/Pt (9.5) > NiOx/Pt (7.5) > bare-Pt (2.3). The a-FeOx/NiOx/Pt and FeOx/NiOx/Pt catalysts had superior catalytic activities; outperforming all the other catalysts. The introduction of nano-NiOx and nano-FeOx could greatly improve the usage of Pt at the unit area level.

In fact, Fig. 5 indicates that the FAOR on the NiOx/Pt catalyst (curve b) showed an improved activity (compare I_p^d) relative to that of the bare Pt catalyst. Furthermore, the catalytic activities of the FeOx/NiOx/Pt and FeOx/Pt catalysts toward the FAOR were much better than those of the NiOx/Pt and bare-Pt catalysts, respectively. That is, I_p^d for the FAOR on the a-FeOx/NiOx/Pt catalyst reached *ca.* 3.1 and 6.2 times higher than that obtained on the NiOx/Pt and bare-Pt catalysts, respectively, and the ratio (I_p^d/I_p^{ind}) of the FAOR increased from 2.3 (on bare-Pt) to 7.5 (on NiOx/Pt) to 11.0 (on FeOx/NiOx/Pt) and 16.5 (on a-FeOx/NiOx/Pt). The a-FeOx/NiOx/Pt and FeOx/NiOx/Pt catalysts exhibited greater FAOR current densities and lower onset potentials; indicating that nano-FeOx boosted the catalytic activity toward the direct FAOR. We believe that nano-NiOx and nano-FeOx could enhance the FAOR reaction *via* a bi-functional mechanism, in which the presence of nano-NiOx and/or nano-FeOx enriched the catalyst's surface with extra oxygen moieties that facilitated the FAOR. Also, the EIS tests and CO stripping experiments (more details are provided below) further revealed that nano-FeOx enhanced the FAOR *via* an electronic effect, allowing a faster electron transport. Obviously, when the deposition order of the modifiers was reversed (*i.e.*, for the NiOx/FeOx/Pt catalyst), I_p^d (21.8 mA cm^{-2}), I_p^d/I_p^{ind} (9.5) and I_p^d/I_b (0.51) increased compared to those of the NiOx/Pt and bare-Pt electrodes. Yet, the catalytic enhancement ($I_p^d/I_p^{ind} = 9.5$) of the former catalyst was still lower than that obtained with the FeOx/NiOx/Pt catalyst ($I_p^d/I_p^{ind} = 11.0$), despite their I_p^d and CO tolerance being nearly the same. The data for the FAOR is summarized in Table 1. It is also interesting to note the competitive performance of the FeOx/NiOx/Pt catalyst, especially after activation, for the FAOR and CO tolerance when compared to the literature data for this reaction (see Table 2).[41,46,56–60]

3.3. Durability of the catalysts

The durability of the investigated catalysts toward the FAOR was tested by measuring current–time (I–t) relations of the FAOR at 0.3 V (Fig. 6). The initial rapid decrease in current demonstrated the poisoning of the electrocatalysts. The current densities of all Pt-modified catalysts were higher than that of the unmodified Pt electrode over continuous electrolysis for 3 h. For all catalysts, the sharp decrease in the current intensity ended with a steady-state current density. The a-FeOx/NiOx/Pt/GC catalyst current density remained nearly constant at *ca.* 4.0 mA cm^{-2} after 3 h of continuous electrolysis, which was nearly fourfold higher than that (1.0 mA cm^{-2}) of the bare-Pt electrode. Among all catalysts, the a-FeOx/NiOx/Pt catalyst maintained the highest current density over the time studied. This suggested that nano-FeOx enhanced the stability and poisoning tolerance of the Pt catalyst.

3.4. Electrochemical impedance spectroscopy (EIS)

The influence of additional modifiers (such as nano-NiOx and/or nano-FeOx) on the charge transport kinetics and the interfacial properties was further investigated using EIS, which is a valuable tool for addressing the results of the FAOR. The charge transfer resistance (R_{ct}) of the prepared electrodes could be used to interpret the charge transfer kinetics of the FAOR. Table 3 compares the different EIS parameters: ohmic resistance (R_s), charge transfer resistance (R_{ct}), constant phase

Open Access Article. Published on 13 July 2022. Downloaded on 11/8/2025 5:17:05 AM.
This article is licensed under a Creative Commons Attribution-NonCommercial 3.0 Unported Licence.

Table 1 Variation of I_p^d, I_p^{ind}, I_b, I_p^d/I_p^{ind}, I_p^d/I_b and E_{onset} for the FAOR as evaluated from Fig. 5

Electrode	I_p^d (mA cm^{-2})	I_p^{ind} (mA cm^{-2})	I_b (mA cm^{-2})	I_p^d/I_p^{ind}	I_p^d/I_b	E_{onset} (mV)
Bare-Pt	4.5	2.0	14.5	2.3	0.31	−74
NiO*x*/Pt	9.0	1.2	14.0	7.5	0.64	−174
FeO*x*/NiO*x*/Pt	22.0	2.0	45.0	11.0	0.49	−186
a-FeO*x*/NiO*x*/Pt	28.0	1.7	38.2	16.5	0.73	−196
NiO*x*/FeO*x*/Pt	21.8	2.3	42.5	9.5	0.51	−82
NiO*x*/a-FeO*x*/Pt	11.5	1.2	23.0	9.6	0.50	−80

Table 2 A comparison of the electrocatalytic activity (I_p^d/I_p^{ind}) and CO tolerance (I_p^d/I_b) toward the FAOR for different catalysts

Electrode	I_p^d/I_p^{ind}	I_p^d/I_b	Ref.
Commercial Pt/C	0.16	—	54
$Pt_{11.1}Ni_{88.9}$/C	0.33	—	54
$Pt_{10.9}Au_{0.2}Ni_{88.9}$/C	0.34	—	54
Pt black	0.24	0.11	55
Pt/C	0.29	0.20	55
PtPd/C	0.87	0.51	55
Pt/GC	0.60	0.19	56
Pt/MWCNTs-GC	7.5	0.45	56
NiO*x*/Pt/GC	3.33	0.40	57
Au/Pt/GC	3.44	0.54	58
Si-TiO*x*/Pt/TiO*x* (700 °C)	10.0	0.67	41
FeO*x*/Pt	9.1	0.58	45
a-FeO*x*/Pt	17.4	0.70	45
FeO*x*/NiO*x*/Pt	11.0	0.49	This work
a-FeO*x*/NiO*x*/Pt	16.5	0.73	This work

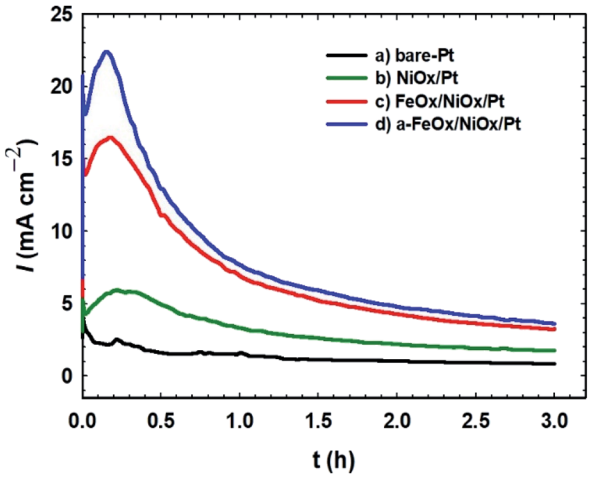

Fig. 6 Current–time transients obtained during the FAOR for the (a) bare-Pt, (b) NiO*x*/Pt, (c) FeO*x*/NiO*x*/Pt and (d) a-FeO*x*/NiO*x*/Pt catalysts in 0.3 mol L^{-1} FA (pH 3.5) at a potential of 0.3 V.

element (CPE) and constant phase coefficient (n) of the various catalysts. The impedance parameters were estimated by fitting the measured EIS data using a Randles equivalent circuit model (inset of Fig. 7). In 0.3 mol L^{-1} FA (pH 3.5), Nyquist and Bode plots were obtained at open circuit potential in the frequency range from 10 mHz to 100 kHz for the bare-Pt, NiO*x*/Pt, FeO*x*/NiO*x*/Pt and a-FeO*x*/NiO*x*/Pt nanocatalysts (see Fig. 7). Interestingly, the diameter of the semicircle for the a-FeO*x*/NiO*x*/Pt electrode was smaller than those obtained for the other prepared catalysts in this investigation. The R_{ct} decreased for these catalysts in the following order: bare-Pt (78.1 kΩ) > NiO*x*/Pt (*ca.* 37.0 kΩ) > FeO*x*/NiO*x*/Pt (25.8 kΩ) > a-FeO*x*/NiO*x*/Pt (15.2 kΩ). This low R_{ct} for the FAOR on the a-FeO*x*/NiO*x*/Pt catalyst was definitely an important element in boosting the reaction kinetics. The different CPE values correlated to the different numbers of active sites at the catalysts' surface; an increase in CPE is directly proportional to an increase in the active sites at the catalyst's surface and, in turn, its activity.[59] Alternatively, when $n = 1$, the CPE can be considered as an ideal capacitor.[60] As expected, all catalysts exhibited a non-ideal behaviour for the double layer, perhaps due to a microscopic inhomogeneity at

Table 3 Impedance parameters obtained during the FAOR for the bare-Pt, NiO*x*/Pt, FeO*x*/NiO*x*/Pt and a-FeO*x*/NiO*x*/Pt electrodes. The data are derived from the corresponding EIS spectra (Fig. 7)

Electrode	R_s [kΩ]	R_{ct} [kΩ]	CPE [μFs$^{(n-1)}$]	n
Bare-Pt	0.354	78.10	1.189	0.9323
NiO*x*/Pt	0.319	36.97	5.177	0.7632
FeO*x*/NiO*x*/Pt	0.975	25.80	3.461	0.8207
a-FeO*x*/NiO*x*/Pt	0.238	15.20	15.880	0.8351

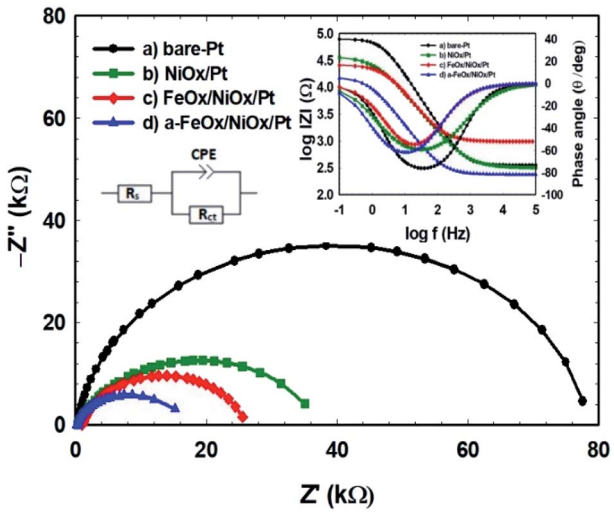

Fig. 7 Nyquist and Bode plots of the FAOR for the (a) bare-Pt, (b) NiO*x*/Pt, (c) FeO*x*/NiO*x*/Pt and (d) a-FeO*x*/NiO*x*/Pt catalysts in 0.3 mol L^{-1} aqueous FA (pH 3.5) at open circuit potential.

 © 2022 The Author(s). Published by the Royal Society of Chemistry

Open Access Article. Published on 13 July 2022. Downloaded on 11/8/2025 5:17:05 AM.
This article is licensed under a Creative Commons Attribution-NonCommercial 3.0 Unported Licence.

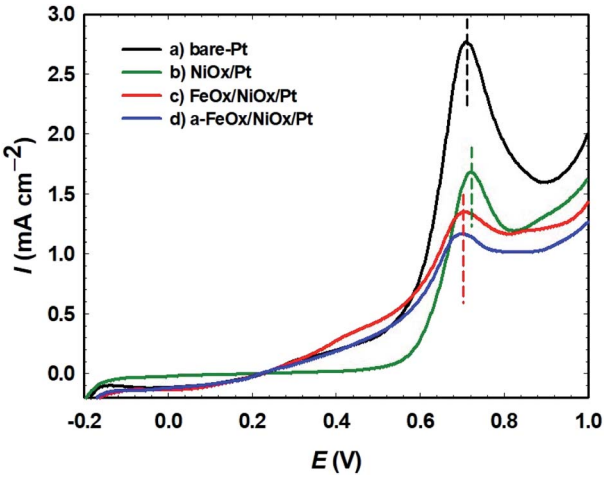

Fig. 8 Oxidative CO stripping for the (a) bare-Pt, (b) NiO*x*/Pt, (c) FeO*x*/NiO*x*/Pt and (d) a-FeO*x*/NiO*x*/Pt electrodes in 0.5 mol L^{-1} H_2SO_4 measured at 50 mV s^{-1}. Before the measurements, CO was adsorbed from 0.5 mol L^{-1} FA at open circuit potential for 10 min.

the electrode surface. It is clear that the a-FeO*x*/NiO*x*/Pt catalyst possessed the highest CPE and catalytic activity values.

3.5. CO stripping

The capability for oxidation of the adsorbed CO with regard to the surface composition of the prepared catalysts was demonstrated using CO stripping analysis (Fig. 8). The desired voltage to drive the maximum CO_{ads} oxidation kinetics was represented by the positions of the CO_{ads} oxidation peaks in a CO stripping curve.[61] In 0.5 mol L^{-1} FA, CO was permitted to adsorb on the surfaces of the bare-Pt, NiO*x*/Pt, FeO*x*/NiO*x*/Pt and a-FeO*x*/NiO*x*/Pt electrodes for 10 min at open circuit potential. The adsorbed CO layer was next stripped electrochemically (oxidatively) in 0.5 mol L^{-1} H_2SO_4 at a potential scan rate of 50 mV s^{-1}, yielding the oxidation peaks displayed in Fig. 8. A sharp peak was detected for the bare-Pt electrode at 0.71 V, with a peak current density of 2.8 mA cm^{-2}. Compared with that of the bare-Pt electrode, the CO stripping voltammogram of the NiO*x*/Pt electrode presented a CO stripping peak at almost the same potential (0.71 V), but with a different amount of CO and peak current intensity (1.7 mA cm^{-2}). On the other hand, the FeO*x*/NiO*x*/Pt and a-FeO*x*/NiO*x*/Pt electrodes showed much lower peak intensities of 1.4 and 1.2 mA cm^{-2} at ~ 0.70 and ~ 0.69 V, respectively. This suggested higher CO tolerance of the FeO*x*/NiO*x*/Pt and a-FeO*x*/NiO*x*/Pt catalysts that was inferred, not only from the lower amounts of adsorbed CO molecules, but also from the slightly negative shift in their peak potentials. This means that nano-FeO*x* participated in the catalysis of the FAOR *via* both the bi-functional and electronic effects.

4. Conclusion

A propitious ternary FeO*x*/NiO*x*/Pt catalyst was synthesized for efficient formic acid electro-oxidation. Compared with the bare-Pt electrode, the FeO*x*/NiO*x*/Pt catalyst demonstrated a better catalytic activity and tolerance against CO poisoning of ~4.8 and 1.6 times, respectively. Activation of this catalyst at −0.5 V in 0.2 mol L^{-1} NaOH led to improvements in the catalytic activity (~7.2 times) and CO tolerance (~2.4 times) compared to the bare-Pt catalyst. Also, the existence of nano-FeO*x* enhanced the durability and E_{onset} of the catalyst for the FAOR. The role of nano-FeO*x* in the catalytic enhancement was interpreted by EIS and CO stripping analyses to be electronic. It also exhibited a bi-functional effect *via* enriching the catalyst surface with extra oxygen moieties that facilitated the FAOR, especially after activation.

Conflicts of interest

There are no conflicts to declare.

References

1 H. Xu, K. Zhang, B. Yan, J. Wang, C. Wang, S. Li, Z. Gu, Y. Du and P. Yang, *J. Power Sources*, 2017, **356**, 27–35.
2 S. Li, J. Lai, R. Luque and G. Xu, *Energy Environ. Sci.*, 2016, **9**, 3097–3102.
3 D. Minudri, A. Y. Tesio, F. Fungo, R. E. Palacios, P. S. Cappellari, E. Pastor and G. A. Planes, *J. Power Sources*, 2021, **483**, 229189.
4 I. M. Al-Akraa, B. A. Al-Qodami and A. M. Mohammad, *Int. J. Electrochem. Sci.*, 2020, **15**, 4005–4014.
5 H. Lee, Y. Sohn and C. K. Rhee, *Langmuir*, 2020, **36**, 5359–5368.
6 S. Luo, W. Chen, Y. Cheng, X. Song, Q. Wu, L. Li, X. Wu, T. Wu, M. Li and Q. Yang, *Adv. Mater.*, 2019, **31**, 1903683.
7 L. Sui, W. An, C. K. Rhee and S. H. Hur, *J. Electrochem. Sci. Technol.*, 2020, **11**, 84–91.
8 Z. Liu, G. Fu, J. Li, Z. Liu, L. Xu, D. Sun and Y. Tang, *Nano Res.*, 2018, **11**, 4686–4696.
9 D. Bhalothia, T.-H. Huang, P.-H. Chou, K.-W. Wang and T.-Y. Chen, *RSC Adv.*, 2020, **10**, 17302–17310.
10 P. Hong, F. Luo, S. Liao and J. Zeng, *Int. J. Hydrogen Energy*, 2011, **36**, 8518–8524.
11 E. Herrero and J. M. Feliu, *Curr. Opin. Electrochem.*, 2018, **9**, 145–150.
12 J. M. Hermann, A. Abdelrahman, T. Jacob and L. A. Kibler, *Electrochim. Acta*, 2021, **385**, 138279.
13 X. Jiang, Y. Liu, J. Wang, Y. Wang, Y. Xiong, Q. Liu, N. Li, J. Zhou, G. Fu and D. Sun, *Nano Res.*, 2019, **12**, 323–329.
14 M. Choi, C.-Y. Ahn, H. Lee, J. K. Kim, S.-H. Oh, W. Hwang, S. Yang, J. Kim, O.-H. Kim, I. Choi, Y.-E. Sung, Y.-H. Cho, C. K. Rhee and W. Shin, *Appl. Catal., B*, 2019, **253**, 187–195.
15 G. H. El-Nowihy and M. S. El-Deab, *Int. J. Hydrogen Energy*, 2020, **45**, 21297–21307.
16 P. S. Cappellari, A. M. Baena-Moncada, R. Coneo-Rodríguez, M. S. Moreno, C. A. Barbero and G. A. Planes, *Int. J. Hydrogen Energy*, 2019, **44**, 1967–1972.
17 Y. M. Asal, A. M. Mohammad, S. S. Abd El Rehim and I. M. Al-Akraa, *J. Saudi Chem. Soc.*, 2022, **26**, 101437.

Open Access Article. Published on 13 July 2022. Downloaded on 11/8/2025 5:17:05 AM.
This article is licensed under a Creative Commons Attribution-NonCommercial 3.0 Unported Licence.

18 L. Zhang, J. V. Perales-Rondón, A. Thomère, J. Blanchard and C. M. Sánchez-Sánchez, *J. Electroanal. Chem.*, 2021, **896**, 115491.
19 T. Al Najjar, N. Ahmed and E. N. El Sawy, *RSC Adv.*, 2021, **11**, 22842–22848.
20 K. Jiang, H.-X. Zhang, S. Zou and W.-B. Cai, *Phys. Chem. Chem. Phys.*, 2014, **16**, 20360–20376.
21 I. M. Al-Akraa, B. A. Al-Qodami, M. S. Santosh, R. Viswanatha, A. K. Thottoli and A. M. Mohammad, *Int. J. Electrochem. Sci.*, 2020, **15**, 5597–5608.
22 S. Luo and P. K. Shen, *ACS Nano*, 2017, **11**, 11946–11953.
23 I. M. Al-Akraa, Y. M. Asal and A. M. Mohammad, *Arabian J. Chem.*, 2022, **15**, 103965.
24 Y. M. Asal, I. M. Al-Akraa, A. M. Mohammad and M. S. El-Deab, *Int. J. Hydrogen Energy*, 2019, **44**, 3615–3624.
25 I. M. Al-Akraa, A. M. Mohammad, M. S. El-Deab and B. E. El-Anadouli, *Int. J. Electrochem. Sci.*, 2012, **7**, 3939–3946.
26 C. Zhai, H. Zhang, J. Hu, L. Zeng, M. Xue, Y. Du and M. Zhu, *J. Alloys Compd.*, 2019, **774**, 274–281.
27 Y. Huang, T. Zhao, L. Zeng, P. Tan and J. Xu, *Electrochim. Acta*, 2016, **190**, 956–963.
28 B. Habibi and N. Delnavaz, *Int. J. Hydrogen Energy*, 2011, **36**, 9581–9590.
29 E. N. El Sawy and P. G. Pickup, *Electrochim. Acta*, 2019, **302**, 234–240.
30 Q. Yi, J. Zhang, A. Chen, X. Liu, G. Xu and Z. Zhou, *J. Appl. Electrochem.*, 2008, **38**, 695–701.
31 W. Chen, J. Kim, S. Sun and S. Chen, *Langmuir*, 2007, **23**, 11303–11310.
32 G. V. Ramesh, R. Kodiyath, T. Tanabe, M. Manikandan, T. Fujita, N. Umezawa, S. Ueda, S. Ishihara, K. Ariga and H. Abe, *ACS Appl. Mater. Interfaces*, 2014, **6**, 16124–16130.
33 G. V. Ramesh, R. Kodiyath, T. Tanabe, M. Manikandan, T. Fujita, F. Matsumoto, S. Ishihara, S. Ueda, Y. Yamashita and K. Ariga, *ChemElectroChem*, 2014, **1**, 728–732.
34 X. Hu, J. Zou, H. Gao and X. Kang, *J. Colloid Interface Sci.*, 2020, **570**, 72–79.
35 Y. Chen, H.-J. Niu, Y.-G. Feng, J.-H. Wu, A.-J. Wang, H. Huang and J.-J. Feng, *Appl. Surf. Sci.*, 2020, **510**, 145480.
36 Y.-X. Wang, C.-F. Liu, M.-L. Yang, X.-H. Zhao, Z.-X. Xue and Y.-Z. Xia, *Chin. Chem. Lett.*, 2017, **28**, 60–64.
37 Y. Xie and N. Dimitrov, *Appl. Catal., B*, 2020, **263**, 118366.
38 G. A. El-Nagar, A. M. Mohammad, M. S. El-Deab and B. E. El-Anadouli, *J. Electrochem. Soc.*, 2012, **159**, F249.
39 G. A. El-Nagar, A. M. Mohammad, M. S. El-Deab and B. E. El-Anadouli, *Electrochim. Acta*, 2013, **94**, 62–71.
40 G. A. El-Nagar, A. M. Mohammad, M. S. El-Deab and B. E. El-Anadouli, in *Progress in Clean Energy*, Springer, 2015, vol. 1, pp. 577–594.
41 I. M. Al-Akraa and A. M. Mohammad, *Arabian J. Chem.*, 2020, **13**, 4703–4711.
42 A. M. Mohammad, I. M. Al-Akraa and M. S. El-Deab, *Int. J. Hydrogen Energy*, 2018, **43**, 139–149.
43 Y. M. Asal, I. M. Al-Akraa, A. M. Mohammad and M. S. El-Deab, *J. Taiwan Inst. Chem. Eng.*, 2019, **96**, 169–175.
44 G. A. El-Nagar, A. M. Mohammad, M. S. El-Deab and B. E. El-Anadouli, *ACS Appl. Mater. Interfaces*, 2017, **9**, 19766–19772.
45 B. A. Al-Qodami, H. H. Farrag, S. Y. Sayed, N. K. Allam, B. E. El-Anadouli and A. M. Mohammad, *J. Nanotechnol.*, 2018, **2018**, 4657040.
46 B. A. Al-Qodami, H. H. Alalawy, I. M. Al-Akraa, S. Y. Sayed, N. K. Allam and A. M. Mohammad, *Int. J. Hydrogen Energy*, 2022, **47**, 264–275.
47 G. A. El-Nagar and A. M. Mohammad, *Int. J. Hydrogen Energy*, 2014, **39**, 11955–11962.
48 L. Chen, L. Liu, Q. Guo, Z. Wang, G. Liu, S. Chen and H. Hou, *RSC Adv.*, 2017, **7**, 19345–19352.
49 M. Nagasaka, H. Yuzawa, T. Horigome, A. P. Hitchcock and N. Kosugi, *J. Phys. Chem. C*, 2013, **117**, 16343–16348.
50 Y.-X. Chen, S.-P. Chen, Q.-S. Chen, Z.-Y. Zhou and S.-G. Sun, *Electrochim. Acta*, 2008, **53**, 6938–6943.
51 M. G. Kim, J. H. Paik and Y. Tak, *J. Nanosci. Nanotechnol.*, 2016, **16**, 10639–10643.
52 A. Godymchuk, I. Papina, E. Karepina, D. Kuznetsov, I. Lapin and V. Svetlichnyi, *J. Nanopart. Res.*, 2019, **21**, 208.
53 A. O. Elnabawy, J. A. Herron, J. Scaranto and M. Mavrikakis, *J. Electrochem. Soc.*, 2018, **165**, J3109.
54 A. Pei, L. Ruan, B. Liu, W. Chen, S. Lin, B. Chen, Y. Liu, L. H. Zhu and B. H. Chen, *Int. J. Hydrogen Energy*, 2020, **45**, 22893–22905.
55 M. S. Çögenli and A. B. Yurtcan, *Int. J. Hydrogen Energy*, 2018, **43**, 10698–10709.
56 I. M. Al-Akraa, Y. M. Asal and S. A. Darwish, A Simple and Effective Way to Overcome Carbon Monoxide Poisoning of Platinum Surfaces in Direct Formic Acid Fuel Cells, *Int. J. Electrochem. Sci.*, 2019, **14**, 8267–8275.
57 I. M. Al-Akraa, A. E. Salama, Y. M. Asal and A. M. Mohammad, *Arabian J. Chem.*, 2021, **14**, 103383.
58 I. M. Al-Akraa, Y. M. Asal and A. M. Mohammad, *J. Nanomater.*, 2019, **2019**, 2784708.
59 R. K. Shervedani and M. Bagherzadeh, *Electrochim. Acta*, 2008, **53**, 6293–6303.
60 W. Chen, J. Kim, S. Sun and S. Chen, *Phys. Chem. Chem. Phys.*, 2006, **8**, 2779–2786.
61 D. Bhalothia, T.-H. Huang, P.-H. Chou, P.-C. Chen, K.-W. Wang and T.-Y. Chen, *Sci. Rep.*, 2020, **10**, 8457.

 © 2022 The Author(s). Published by the Royal Society of Chemistry